

Parallel-Plate Electrostatic Dual-Mass Oscillator

Christopher W. Dyck⁺, James J. Allen, and Robert, J. Huber

Intelligent Micromachines
Sandia National Laboratories
MS 1080, PO Box 5800
Albuquerque, NM 87185-1080

RECEIVED

AUG 11 1999

ABSTRACT

OSTI

A surface-micromachined two-degree-of-freedom system that was driven by parallel-plate actuation at antiresonance was demonstrated. The system consisted of an absorbing mass connected by folded springs to a drive mass. The system demonstrated substantial motion amplification at antiresonance. The absorber mass amplitudes were 0.8 - 0.85 μm at atmospheric pressure while the drive mass amplitudes were below 0.1 μm . Larger absorber mass amplitudes were not possible because of spring softening in the drive mass springs. Simple theory of the dual-mass oscillator has indicated that the absorber mass may be insensitive to limited variations in strain and damping. This needs experimental verification. Resonant and antiresonant frequencies were measured and compared to the designed values. Resonant frequency measurements were difficult to compare to the design calculations because of time-varying spring softening terms that were caused by the drive configuration. Antiresonant frequency measurements were close to the design value of 5.1 kHz. The antiresonant frequency was not dependent on spring softening. The measured absorber mass displacement at antiresonance was compared to computer simulated results. The measured value was significantly greater, possibly due to neglecting fringe fields in the force expression used in the simulation.

Keywords: Surface Micromachining, Resonator, Actuator, Vibration Absorber, Motion Amplifier.

1. INTRODUCTION

Presently, there is a need in surface micromachining for a resonator that is capable of large motions at low drive voltages. Large, linear displacements are obtained by using comb drive actuation, however the force of a comb drive is low and large drive voltages are needed. Parallel-plate drive actuation generates larger forces over a comparable area, however the displacement is limited because the force is nonlinear.

The dual-mass oscillator provides a potential solution to the problem. By forcing a two-degree-of-freedom (2DOF) system at antiresonance, parallel-plate actuation may be used to obtain displacements that exceed 1/3 of the electrode gap. This system operates on the same principle as the dynamic vibration absorber¹. An absorber spring-mass system is connected to a system that is experiencing unwanted oscillations. If the resonant frequency of the absorber spring-mass system matches the frequency of the unwanted oscillations, the absorber mass will act to oppose the force causing the oscillation, rendering the original oscillating system stationary. Bulk micromachined structures have been fabricated to demonstrate this concept in the form of base driven structures², and a torsional resonator³.

The objectives of this paper are to demonstrate the operation of the dual mass resonator, and to compare some preliminary results to the design calculations. The theory section presents the design and analysis equations, and some interesting characteristics of the dual-mass oscillator. The oscillation amplitude appears to be insensitive to limited variations in damping and strain. The design section summarizes the calculations of the prototype structure's parameters. Observations of the functioning dual-mass oscillator were made. Preliminary measurements of resonant and antiresonant frequencies were also recorded to compare the fabricated structure to the design calculations. Absorber mass displacement measurements were also taken to compare to a computer solution. The results were discussed and summarized in the last two sections of the paper.

⁺ Contact Information: Email: cdyck@sandia.gov; Website: www.sandia.mdl.gov/Micromachine, Tel: (505) 845-7743, Fax: (505) 844-2991. Under contract with the University of New Mexico, CHTM

DISCLAIMER

This report was prepared as an account of work sponsored by an agency of the United States Government. Neither the United States Government nor any agency thereof, nor any of their employees, make any warranty, express or implied, or assumes any legal liability or responsibility for the accuracy, completeness, or usefulness of any information, apparatus, product, or process disclosed, or represents that its use would not infringe privately owned rights. Reference herein to any specific commercial product, process, or service by trade name, trademark, manufacturer, or otherwise does not necessarily constitute or imply its endorsement, recommendation, or favoring by the United States Government or any agency thereof. The views and opinions of authors expressed herein do not necessarily state or reflect those of the United States Government or any agency thereof.

DISCLAIMER

Portions of this document may be illegible in electronic image products. Images are produced from the best available original document.

2. THEORY

The steady-state equations of the dual mass resonator are presented for design and analysis of the system. A lumped parameter model is assumed. Antiresonance is defined, and the strain and damping insensitivity are discussed.

A diagram of a 2DOF system is shown Fig 1. m_1 is connected through a spring (k_1) to the substrate, and m_2 is connected through a spring (k_2) to m_1 . m_1 and m_2 are often referred to in this paper as the drive mass and the absorber mass, respectively, k_1 and k_2 are often referred to as the drive mass spring and the absorber mass spring. c_1 and c_2 are viscous damping coefficients. Damping between the two masses has been neglected because it is easily designed out of the system. x_1 and x_2 are measured relative to the substrate. The equations of dynamics for Fig. 1 are

$$m_1 \ddot{x}_1 + c_1 \dot{x}_1 + k_1 x_1 + k_2 (x_1 - x_2) = F \quad (1)$$

$$m_2 \ddot{x}_2 + c_2 \dot{x}_2 + k_2 (x_2 - x_1) = 0. \quad (2)$$

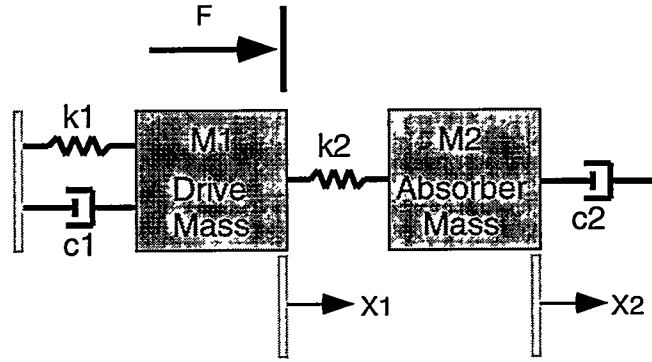


Figure 1: Diagram of a 2DOF system. Damping between m_1 and m_2 has been neglected.

The steady-state responses of the 2DOF system to a time-varying sinusoidal input force, $F = F_o \sin \omega t$ are

$$\frac{X_1}{F_o} = \frac{1}{k_1} \frac{1 - \left(\frac{\omega}{\omega_{22}}\right)^2 + j\omega \frac{c_2}{k_2}}{\left[1 + \frac{k_2}{k_1} - \left(\frac{\omega}{\omega_{11}}\right)^2 + j\omega \frac{c_1}{k_1}\right] \left[1 - \left(\frac{\omega}{\omega_{22}}\right)^2 + j\omega \frac{c_2}{k_2}\right] - \frac{k_2}{k_1}} \quad (3)$$

and

$$\frac{X_2}{F_o} = \frac{1}{k_1} \frac{1}{\left[1 + \frac{k_2}{k_1} - \left(\frac{\omega}{\omega_{11}}\right)^2 + j\omega \frac{c_1}{k_1}\right] \left[1 - \left(\frac{\omega}{\omega_{22}}\right)^2 + j\omega \frac{c_2}{k_2}\right] - \frac{k_2}{k_1}} \quad (4)$$

where

$$\omega_{11} = \sqrt{k_1/m_1} \quad \text{and} \quad \omega_{22} = \sqrt{k_2/m_2} \quad (5)$$

are the resonant frequencies of the isolated m_1 - k_1 and m_2 - k_2 systems, and not the 2DOF system resonant frequencies. This notation was borrowed from Thompson⁴.

The amplitude and phase of Eq. (3) and Eq. (4) are plotted in Fig. 2. There are three frequencies of interest: two resonant frequencies, f_{o1} and f_{oh} , and an antiresonant frequency, f_{22} . Figure 2 shows that at $f = f_{o1}$, X_1 and X_2 are in phase, and at $f = f_{oh}$, X_1 and X_2 are 180° out of phase. The system resonant frequencies are approximated by equating the denominators of the *undamped* system responses to zero,

$$\left[1 + \frac{k_2}{k_1} - \left(\frac{\omega}{\omega_{11}} \right)^2 \right] \left[1 - \left(\frac{\omega}{\omega_{22}} \right)^2 \right] - \frac{k_2}{k_1} = 0. \quad (6)$$

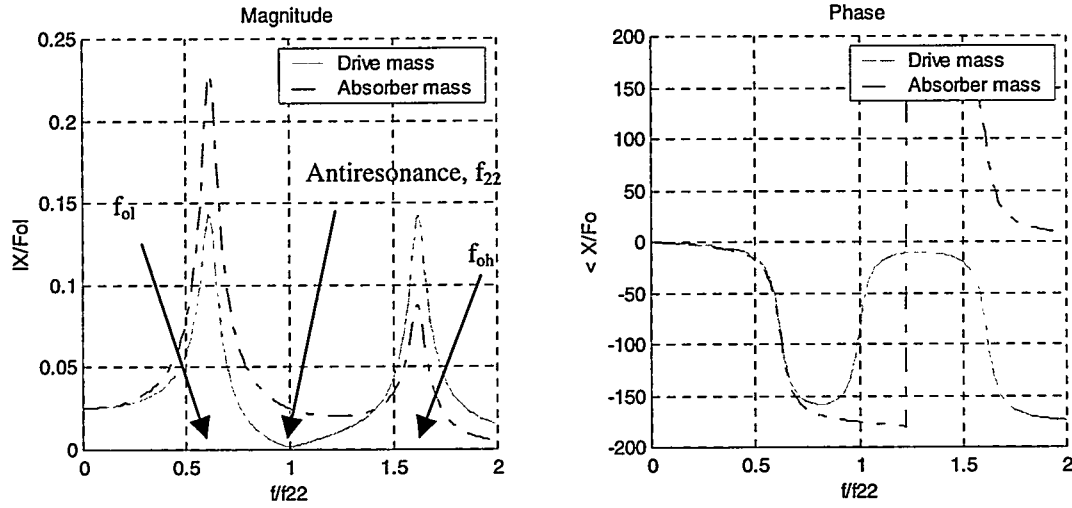


Figure 2: Amplitude and phase frequency responses for a two-degree-of-freedom system.

The solutions to Eq. (6) are

$$\frac{\omega}{\omega_{22}} = \frac{f}{f_{22}} = \sqrt{\frac{1}{2} \left\{ \frac{1}{\gamma^2} + (1 + \mu) \pm \sqrt{\left[\frac{1}{\gamma^2} + (1 + \mu) \right]^2 - \frac{4}{\gamma^2}} \right\}^{1/2}}, \quad (7)$$

where μ is the mass ratio, m_2/m_1 , and γ is the frequency ratio, f_{22}/f_{11} . f_{ol} and f_{oh} are dependent on μ . As μ decreases, the resonant frequency separation decreases; an important point to keep in mind when designing the dual-mass oscillator. This is shown in Fig. 3 where Eq. (7) is plotted as a function of μ , assuming $\gamma=1$. The resonant frequencies, f_{ol} and f_{oh} should be separated far enough such that variations in the drive frequency away from $f = f_{22}$, do not cause significant changes in the absorber mass amplitude.

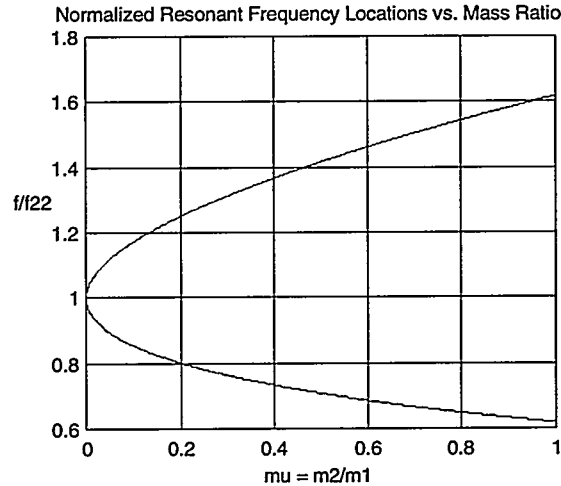


Figure 3: Mode dependence on the mass ratio.

Figure 2 shows that when $f = f_{22}$, $|X_1|$ is a minimum value (between f_{ol} and f_{oh}). The phase response in Fig. 2 shows that X_1 and X_2 are 90° out of phase at $f = f_{22}$. This frequency is defined as *antiresonance*. $|X_1|$ is a minimum here because the absorber mass, m_2 is moving such that it opposes the input force, F on the drive mass, m_1 . X_2 is 180° out of phase with F . In

the absence of damping, $|X_1| = 0$, and the absorber mass exactly cancels the effects of the input force, F . In the presence of damping, $|X_1|$ is finite. The absorber mass dissipates energy because $c_2 \neq 0$. This energy loss must be supplied by the source to the system, and m_1 begins to move.

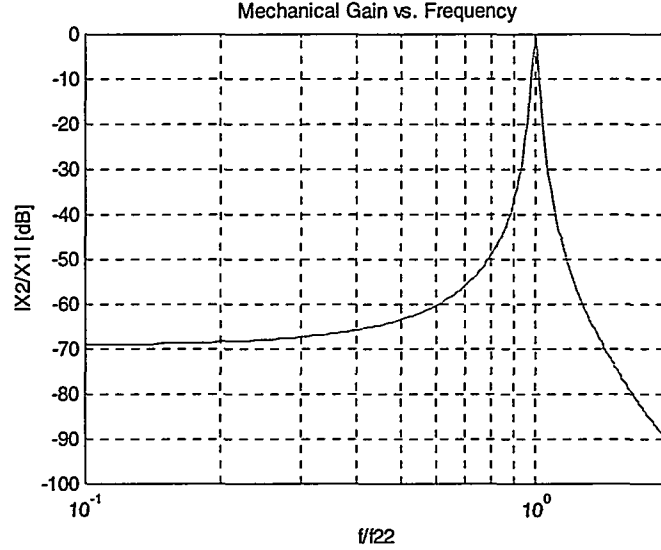


Figure 4: Mechanical gain, $|X_2/X_1|$. This reaches a maximum at $f = f_{22}$.

Antiresonance is also defined as the frequency where the mechanical gain, $|X_2/X_1|$ is a maximum. The mechanical gain is found by dividing Eq. (4) by Eq. (3),

$$\left| \frac{X_2}{X_1} \right| = \frac{1}{1 - \left(\frac{\omega}{\omega_{22}} \right)^2 + j\omega \frac{c_2}{k_2}}. \quad (8)$$

This is plotted in Fig. 4. At $f = f_{22}$, Eq. (8) reduces to

$$\left| \frac{X_2}{X_1} \right| = \frac{k_2}{\omega_{22} c_2}. \quad (9)$$

The mechanical gain is infinite in the absence of damping, and it decreases with increasing damping of the absorber mass, m_2 . This presents another way of viewing the dual-mass oscillator: as a mechanical amplifier. At atmospheric pressure calculations show that the mechanical gain is approximately 10 – 50 for surface micromachined devices, although this is variable depending on the geometry of the structure.

Calculations show that dual-mass oscillator designs are possible that allow X_2 to be independent of damping and changes in k_1 , the drive mass spring. At antiresonance, the denominator of Eq. (4) (and Eq. (3)) reduces to

$$k_1 \left[1 + \frac{k_2}{k_1} - \left(\frac{\omega_{22}}{\omega_{11}} \right)^2 + j\omega_{22} \frac{c_1}{k_1} \right] \left(j\omega_{22} \frac{c_2}{k_2} \right) - k_2, \quad (10)$$

or with the dimensionless constants, μ and γ , described earlier,

$$-\left(k_2 + \frac{c_1 c_2}{m_2} \right) + j\omega_{22} c_2 \left[\frac{1}{\mu} \left(\frac{1}{\gamma^2} - 1 \right) + 1 \right]. \quad (11)$$

Under conditions of low damping, Eq. (11) reduces to $-k_2$, and the displacement of the absorber mass becomes, $X_2 = -F_0/k_2$. The amplitude, $|X_2|$ is insensitive to c_1 , c_2 , and k_1 . At atmospheric pressure, this is still true, but the range of insensitivity is limited. Calculations have shown that practical designs are possible at atmospheric pressure. For example, assume $f_{22} = 5$ kHz, $k_2 = 1$ N/m, and $\mu = 1$. The magnitude of Eq. (11) is plotted in Fig. 5 as a function of $\gamma = f_{22}/f_{11}$ for varying values of c_1

$= c_2 = c$ from 10^{-6} N/m/s to 10^{-5} N/m/s. Figure 5 shows that for $\gamma = 2$ the denominator is independent of γ , and that for an order of magnitude change in the damping coefficients, the denominator magnitude varies by 10 %.

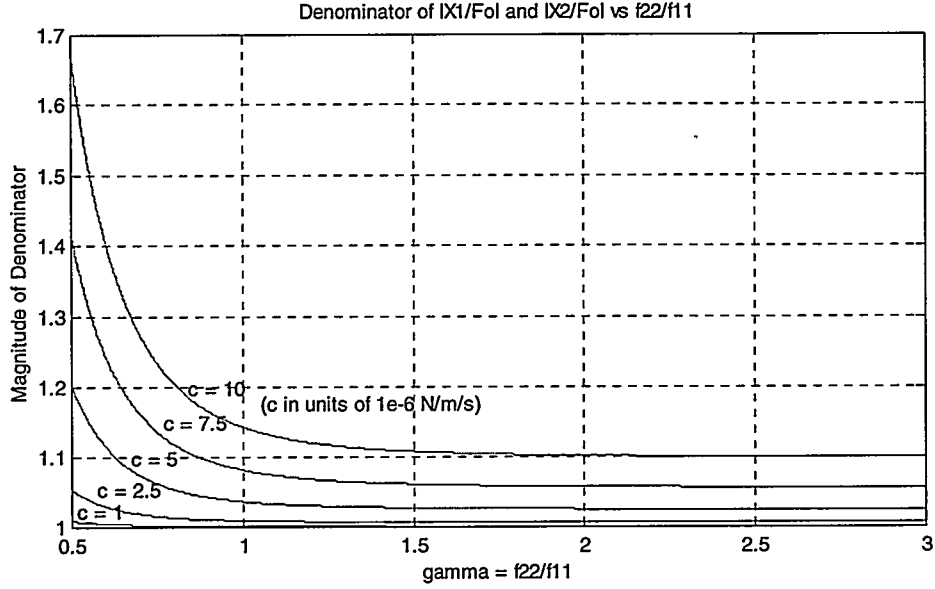


Figure 5: $|X_2|$ vs. $\gamma = f_{22}/f_{11}$, for varying damping coefficient values ($c = c_1 = c_2$).

3. DESIGN

The 2DOF structure in Fig. 6 was designed as a prototype dual-mass oscillator. The absorber mass (inner mass) was suspended by four folded flexures to the drive mass (outer mass), and the drive mass was anchored to the substrate by four straight beams. The drive mass had several windows etched into its sides and ends. Fixed electrodes were patterned within these windows to electrostatically drive the dual-mass oscillator. This structure was fabricated out of polycrystalline silicon (polysil) using the first two levels of the 4-level SUMMiT surface micromachining process⁵.

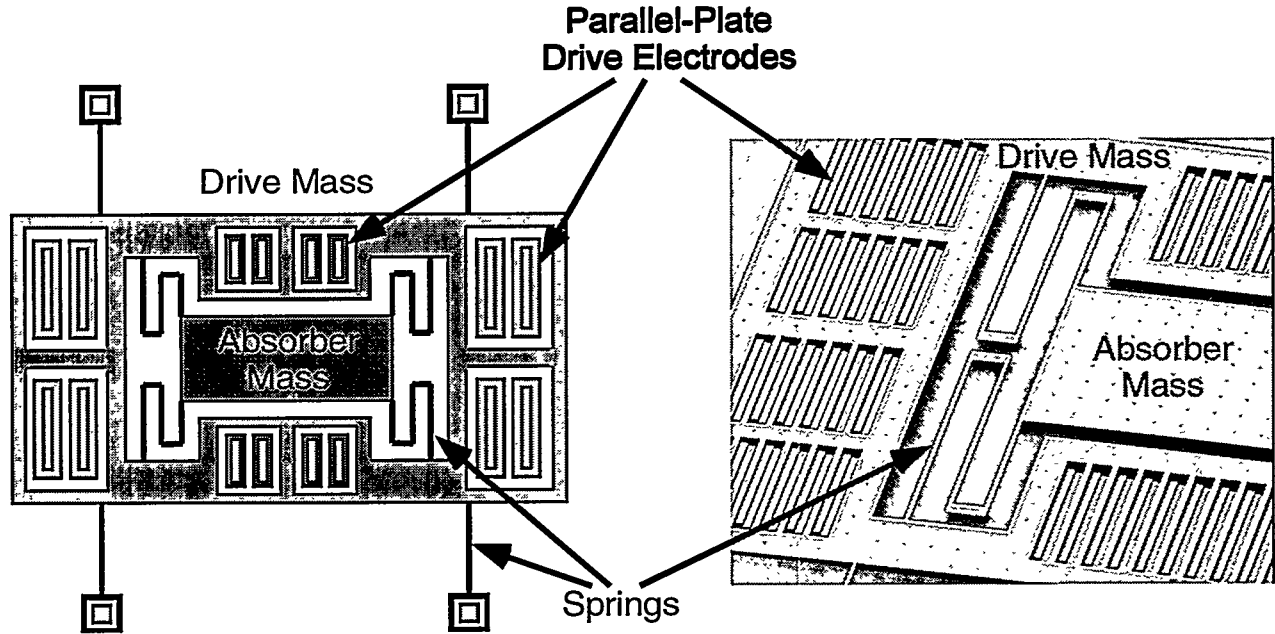


Figure 6: Prototype design of dual-mass oscillator. The antiresonant frequency was designed for, $f_{22} = 5.1$ kHz.

The design parameters follow and are summarized in Table 1: the absorber mass was $200 \times 450 \mu\text{m}^2$. Assuming a density of polysil, $\rho = 2.33 \text{ g/cm}^3$ and a thickness, $h = 2.45 \mu\text{m}$, $m_2 = 5.14 \times 10^{-10} \text{ kg}$. The folded flexure, $k_2 = 0.53 \text{ N/m}$,

which resulted in $f_{22} = 5.1$ kHz. k_2 was calculated by finite element methods (FEM) using a program written for Matlab. A Young's modulus of 160 GPa and a Poisson's ratio of 0.26 were assumed. The drive mass had 24 parallel-plate electrode pairs on each end, and 15 parallel-plate electrode pairs on each side. The total length of $\frac{1}{2}$ of all of the electrodes was, $l = 9.37$ mm, and the electrode-drive mass gap, $g_0 = 2$ μm . The mass of the drive mass was, $m_2 = 14.6 \times 10^{-10}$ kg, resulting in a mass ratio of $\mu = 0.35$. This ratio was large enough to keep the resonant frequencies separated. From Eq. (7), $f_{o1} = 3.66$ kHz and $f_{oh} = 6.7$ kHz. $c_2 = 0.81 \times 10^{-6}$ N/m/s was calculated assuming couette flow damping on the absorber mass, an air of viscosity 1.8×10^{-5} Ns/m², and a vertical gap between the absorber mass and the substrate of $z_0 = 2$ μm . $c_1 = 4.0 \times 10^{-6}$ N/m/s was calculated assuming both couette flow and squeeze film damping⁶ between the drive mass and the fixed electrodes. The ratio $\gamma = f_{11}/f_{22} \approx 1$ was specified after plotting $|X_2|$ as a function of γ (Fig. 7). For $\gamma \leq 1$, $|X_2|$ becomes less sensitive to strain and damping variations. Using the FEM program again, the spring constant of the outer beams was, $k_1 = 1.32$ N/m, resulting in $f_{11} = 4.8$ kHz. The design parameters were substituted into Eq. (3) and (4) and a frequency response was generated in Fig. 8. The mechanical gain at antiresonance was calculated using Eq. (9) to be 21.

Table 1: Design parameters

Parameter	Value	Parameter	Value
L	9.37mm	f_{11}	4.8 kHz
g_0	2 μm	f_{22}	5.1 kHz
k_1	1.3 N/m	γ	1.06
k_2	0.54 N/m	f_{o1}	3.66 kHz
m_1	5.14×10^{-10} kg	f_{oh}	6.7 kHz
m_2	14.6×10^{-10} kg	c_1	4.0 N/m/s
μ	0.35	c_2	0.81 N/m/s

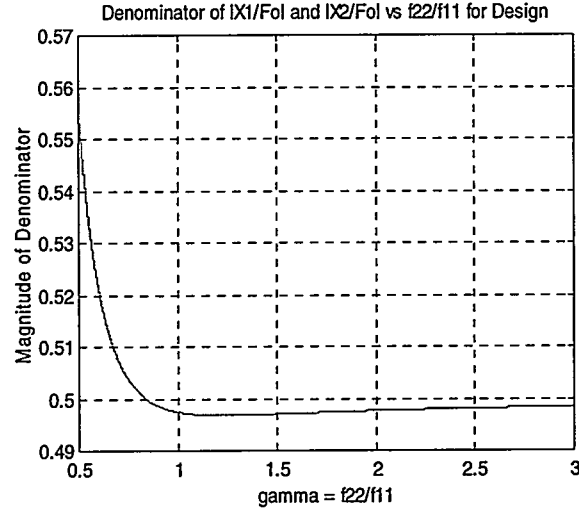


Figure 7: $|X_2|$ vs. $\gamma = f_{22}/f_{11}$ for design parameters listed in Table 1.

4. RESULTS

Prior to the measurements, the behavior of the structure was observed at antiresonance to verify its operation. Measurements and computer solutions were then made to compare the design to the fabricated structures. Antiresonant frequencies, absorber mass amplitudes at antiresonance, and the system resonant frequencies were measured. Equations (1) and (2) were solved by computer for the absorber mass steady-state amplitude at antiresonance.

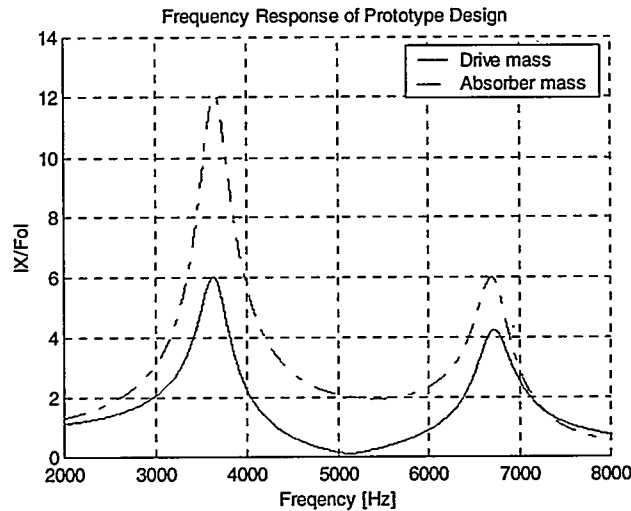


Figure 8: Frequency response of the dual-mass oscillator design using the parameters listed in Table 1.

4.1 Test Setup

The samples were viewed using a 20X objective with a 2X zoom capability on a Mitutoyo microscope that was mounted to a Signatone bench probe station. Two light sources illuminated the samples: a constant illumination white light source and an Olympus Syncrolux Stroboscopic white light source. A Panasonic GP-KR222 CCD camera was mounted to the microscope and connected to a Sony monitor to observe motion of the samples. Displacements were measured on the monitor with a Boekler VIA100 video measuring unit that was calibrated using a stage micrometer. The samples were driven by a HP 8116A 50 MHz function generator. This was connected to a Textronic oscilloscope to verify the drive signal amplitudes. This setup is shown in a Fig. 9.

It was necessary to take measurements of devices that were oscillating in the kHz range. This was done by aliasing the image of the devices using the stroboscopic source. The strobe source was capable of an illumination frequency of 200 Hz, causing the image on the monitor to be an aliased version of the actual image. The strobe frequency was varied to change the oscillation rate of the aliased image to a rate that facilitated taking measurements. This occurred when the actual frequency of the device was close to an integer multiple of the strobe frequency.

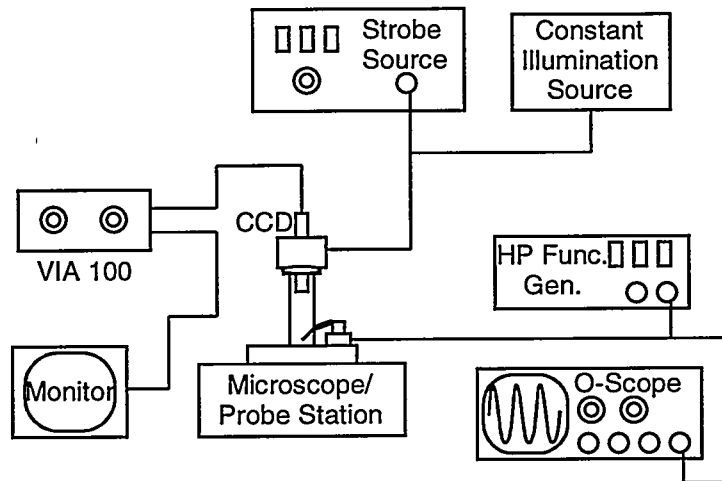


Figure 9: Test setup

4.1 Procedure & Results

Initially there was some difficulty in driving the structures. The structures were driven in a double-sided drive configuration shown in Fig. 10. The ac signals were 180° out of phase, and $V_{dc} \gg V_{ac}$. This configuration did not work

well. The structures clamped to the substrate when V_{dc} exceeded approximately 2 Volt. The drive configuration was changed to a single-sided drive (Fig. 10) and the structures did not clamp to the substrate. This configuration was used for the remaining measurements.

The behavior of several structures operating at antiresonance was observed. The absorber mass, m_2 displaced measurably, however the amplitude of the drive mass, $|X_1|$ was below the measurable limits of our test setup (about 0.1 μm). It was very difficult to find the precise location of antiresonance because the absorber mass amplitude around $f = f_{22}$ was insensitive to frequency changes. An error of $f_{22} \pm 200$ Hz was estimated. The antiresonant frequencies of 6 structures were measured and are recorded in Table 2. The absorbing mass amplitudes of 2 devices operating at antiresonance were also measured and are recorded in Table 3.

Instability in the system was observed that was most likely due to the nonlinear drive force of the parallel-plate electrodes. As the drive voltage was increased to increase the absorber mass amplitude, the drive mass clamped to the drive electrodes. This occurred over a range of 4.2 – 4.7 Volt for all of the devices.

The resonant frequencies of two devices were measured and are recorded in Table 2. f_{ol} and f_{oh} were measured by sweeping the drive frequency and recording the frequency where the structures exhibited maximum displacements. The phase relations between X_1 and X_2 were not measured precisely at these frequencies, however at $f = f_{ol}$ the devices appeared to be in phase and at $f = f_{oh}$ the devices appeared to be 180° out of phase. The drive voltages that were applied during the measurements were recorded for one of the two devices.

Table 2: Frequency measurements

Device #	f_{22} [kHz]	f_{ol} [kHz]	f_{oh} [kHz]
1	5.68	2.5	6.4
2	5.4		
3	5.15		
4	5.15		
5	5.15		
6	4.85	3.45 (2.5 V)	6.55 (2.8 V)

Table 3: Amplitudes at antiresonance.

Drive Signal	$ X_2 $ at $f = f_{22}$ [μm]
$4.2 \sin(\omega_{22}t)$	0.8
$4.6 \sin(\omega_{22}t)$	0.85

Equations (1) and (2) were solved using Matlab's ODE solvers to compare to the results given in Table 3. The force, F in Eq. (2) is given by

$$F = \frac{1}{2} \frac{\partial C}{\partial x} V^2. \quad (12)$$

This is the attractive force between two electrodes with voltage difference, V , separated by a dielectric. The capacitance between the electrodes is C . Neglecting fringe fields and assuming a single-sided drive configuration of $V = V_o \sin(\omega_{22}t)$, Eq. (12) becomes

$$F = \frac{1}{2} \frac{\epsilon_o h l}{(g_o - x)^2} [V_o \sin(\omega_{22}t)]^2. \quad (13)$$

Equation (13) was substituted into Eq. (1). The steady-state response of $|X_2|$ is shown in Figure 11. This response was calculated assuming a drive voltage amplitude, $V_o = 4.2$ Volt and the parameters in Table 1. The absorber mass amplitude in Fig. 11 is approximately 0.5 μm , significantly lower than the measured absorbing mass amplitude in the first entry of Table 3.

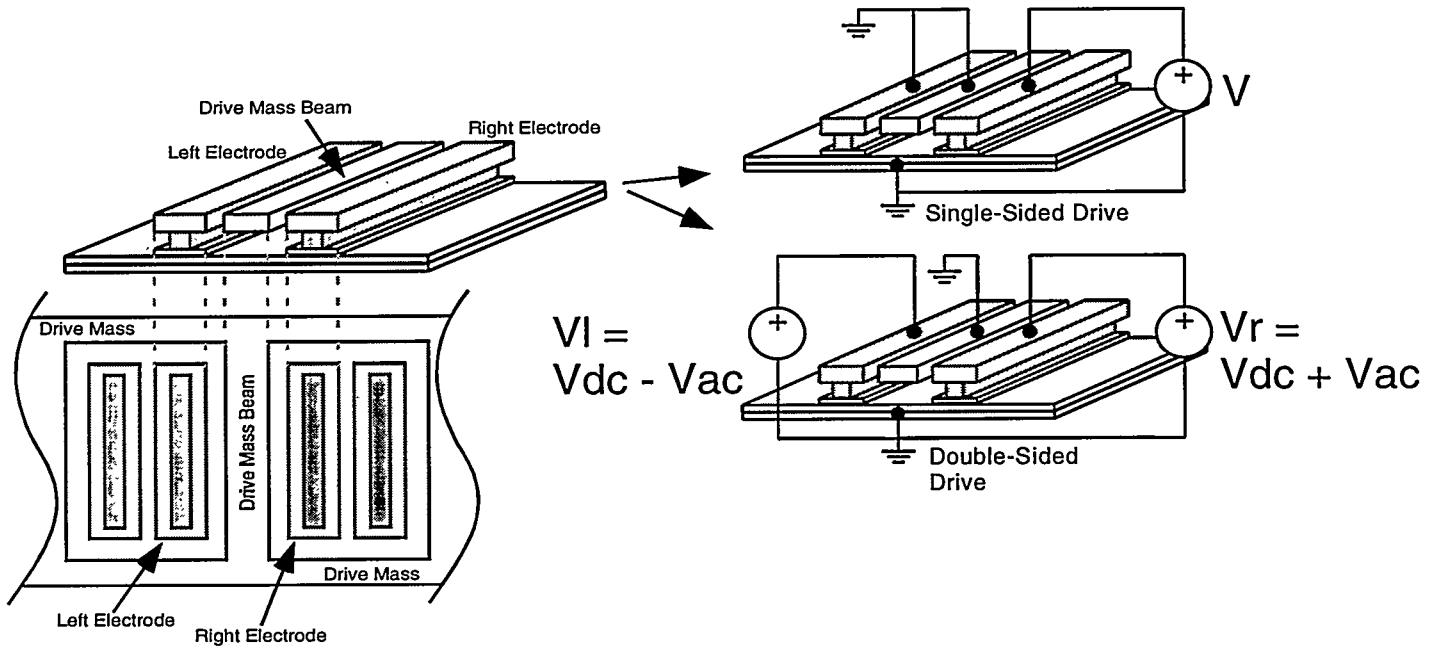


Figure 10: Single-sided and double-sided drive configurations illustrated on a single drive mass parallel-plate electrode.

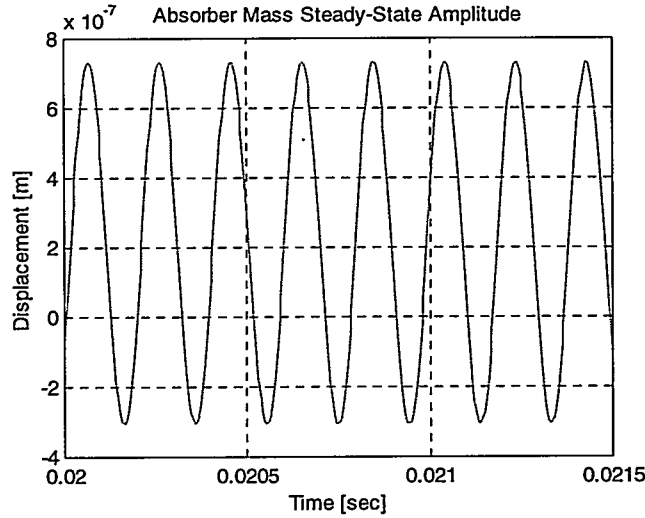


Figure 11: Steady-state response of the absorber mass solved using Matlab's ODE solvers and the calculated design parameters in Table 1.

5. DISCUSSION

Operation of the dual-mass oscillator was demonstrated. Mechanical amplification of the structure was clearly observed at antiresonance. The amplitude of the absorber mass was $0.8 - 0.85 \mu\text{m}$, while the amplitude of the drive mass was below $0.1 \mu\text{m}$. The device also exhibited behavior that was consistent with the frequency response in Fig. 8. The precise location of the antiresonant frequency was difficult to measure indicating that the region of the frequency response near antiresonance was relatively flat.

Larger displacements were attempted but were not possible because the drive mass clamped to the drive electrodes. This was caused by spring softening in k_1 . The prototype structure was designed with $f_{11} \approx f_{22}$, and spring softening was not accounted for. Future designs will have stiffer k_1 values, such that f_{11} can be tuned down during operation to $f_{11} \approx f_{22}$.

Despite the small amplitudes, the concept was demonstrated that parallel-plate actuation can be used to drive structures beyond 1/3 of the electrode gap.

The dual-mass oscillator clamped to the substrate when the double-sided drive was used. It is possible that this was caused by conduction in the silicon-rich SiN layer on the top surface of the substrate. The areas under the drive mass beams were not protected by a ground plane layer, as mentioned in the design section. The double-sided drive signals were $V = V_{dc} + V_{ac}$ and $V = V_{dc} - V_{ac}$ for the electrode pairs. If the SiN layer had been conductive, the region under the drive mass beams would have been held to V_{dc} , increasing the chances that the structure could have been pulled into contact with the substrate. Experiments to determine the conductivity of the silicon-rich SiN produced in our laboratory need to be conducted. This argument, unfortunately does not completely explain why the single-sided drive did not cause the structures to clamp to the substrate. Future designs will include a conductive polysi plane under the drive mass beams that should solve this problem.

Comparisons of the design to the fabricated structures produced mixed results. The measured antiresonant frequencies were close to the calculated values. The average measured antiresonant frequency was 5.23 kHz (Table 2), compared to the design value of 5.1 kHz (Table 1). The measured resonant frequencies were below the calculated values of $f_{ol} = 3.66$ kHz and $f_{oh} = 6.7$ kHz. This was most likely due to spring softening of k_1 inherent in the nonlinear parallel-plate electrostatic drive. f_{ol} and f_{oh} are dependent on k_1 , however f_{22} is not in this design. The measured displacement of the absorber mass at antiresonance was 0.8 μm , significantly above the computer simulated value of 0.5 μm . The discrepancy here was attributed to the parallel-plate electrostatic force term used in the computer simulation. This term neglected fringe fields.

An attempt was made to compare the measured and calculated resonant frequencies by incorporating spring softening terms into the calculated values of the resonant frequencies. This turned out to be difficult because of the nature of the drive configuration that was used when the measurements were taken. The single-sided drive configuration caused the spring softening term to be time varying. This was apparent after manipulating the equation for the single-sided drive force given in Eq. (13). Since measurements of the dual-mass oscillator showed that $|X_1|$ was small with respect to g_o , $\partial C/\partial x$ was approximated by retaining the first two terms in the Taylor series expansion,

$$\frac{\partial C}{\partial x} = \frac{\epsilon_o h l}{g_o^2} \left(1 + \frac{2}{g_o} x \right). \quad (14)$$

This was substituted into Eq. (13), which was rearranged resulting in a force of

$$F = \frac{\epsilon_o h l}{2 g_o^2} \left[\left(\frac{V_o^2}{2} - \frac{V_o^2}{2} \cos 2\alpha x \right) + \frac{2}{g_o} \left(\frac{V_o^2}{2} - \frac{V_o^2}{2} \cos 2\alpha x \right) x \right]. \quad (15)$$

The second term in Eq. (15) added directly to k_1 in Eqs. (3) and (4), making it time varying because of the $\cos 2\alpha x$ term. If the double-sided drive configuration had been used for the resonant frequency measurements, this would not have been a problem. This is seen by using the approach just described. This resulted in a force of

$$F = \frac{\epsilon_o h l}{2 g_o^2} \left[4 V_{dc} V_{ac} + \frac{4}{g_o} (V_{dc}^2 + V_{ac}^2) x \right]. \quad (16)$$

If $V_{dc} \gg V_{ac}$, the time-varying term in Eq. (16) (V_{ac}) is negligible, and the spring softening term is a dc term. Since V_{dc} is known, the spring softening term is known and can be incorporated into the equations for f_{ol} and f_{oh} to compare these frequencies to the design values.

Because of the difficulty in dealing with a time-varying spring constant, the possibility of neglecting the spring softening terms altogether was explored. Unfortunately, this could not be done with confidence. The resonant frequencies of the dual-mass oscillator had been designed such that their dependence on f_{11} was large. This is seen in Fig. 12 where f_{ol} and f_{oh} are plotted as a function of $\gamma = f_{22}/f_{11}$. f_{ol} and f_{oh} have been normalized to f_{22} , and the parameters from Table 1 have been used in this plot. When $\gamma \leq 1$, the slope of the f_{oh} increases dramatically. When $\gamma \approx 1$, the slope of the f_{ol} curve is roughly at it's greatest value. A small change in k_1 in the structure could have caused a large change in f_{ol} and f_{oh} , depending on the design.

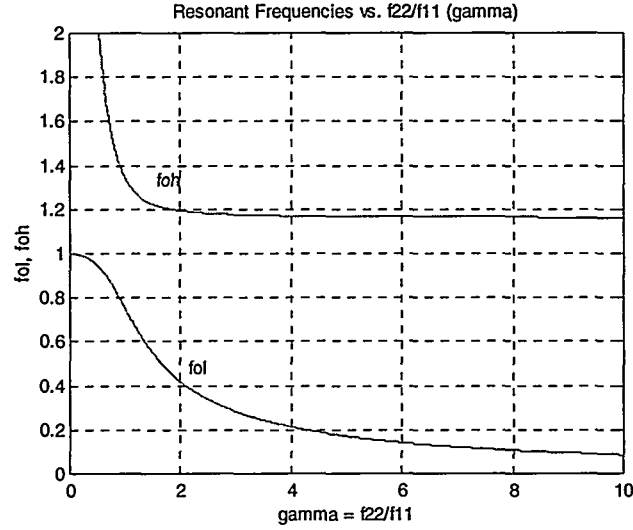


Figure 12: f_{ol} and f_{oh} vs. γ .

To add to the uncertainty, the exact location γ was not known. In this design $\gamma = 1.06$ (Table 1) was calculated. Figure 8 shows that this is close to a region of large change in f_{oh} . The maximum spring softening value of device 6 in Table 1 was 0.16 N/m. This was calculated by substituting the parameters in Table 1 and $V_o = 2.5$ Volt into the second term of Eq. (15). This represented a 6 % change in γ . For $\gamma = 1.06$, spring softening could probably have been ignored without introducing a large error between the calculated mechanical resonant frequencies and the measured resonant frequencies. Unfortunately, the fabricated device's value of γ was not really known because of process variation. In Table 2, the applied voltages for the resonant frequency measurements of device 3 were not recorded. It is possible that either the applied drive voltage was greater in measuring f_{oh} this device than it was for measuring device 6, or that γ was less for this device than for device 3. A combination of both is also possible, as well. Future designs will allow for the double-sided drive. This should make comparisons between the design and fabricated structures much easier.

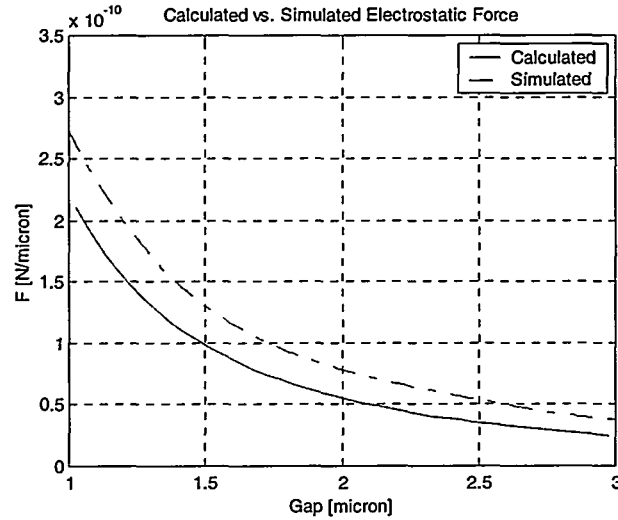


Figure 13: Simulated and calculated force between two parallel conductive beams of height, $h = 2\mu\text{m}$.

Comparison of the measured amplitude, $|X_2|$ in the second entry of Table 3 with the simulated steady-state amplitude in Fig. 7 indicated a large discrepancy between the measured and simulated values. This was believed to be caused by the drive force expression in Eq. (13) that was used in the simulations. This expression neglected fringe fields in the calculation of $\partial C/\partial x$. The electrode gap, g_o and the electrode height, h (Table 1) in the design are close enough such that this significantly underestimated the actual electrostatic force. To demonstrate this, simulations to find the parallel-plate electrostatic force of two parallel beams with $h = 2\mu\text{m}$ were performed using Matlab's Partial Differential Equation (PDE) Solver Toolbox. A curve fit of the simulated force is plotted in Fig. 13 as a function of the beam separation in μm . An arbitrary voltage

difference of 5 Volts was applied between the two beams. As expected, when $x \gg h$ the percentage error between the simulated and calculated forces was much larger, and when $x \ll h$, the error was much smaller. At large separations, the field profile approaches that of two oppositely charged point sources (when viewed from a cross-section). At small separations, the fringe fields were negligible. At $x = 2 \mu\text{m}$, the simulated force was approximately 40 % larger than the calculated force. The geometry of the dual-mass oscillator is significantly more complex than this example, however fringe fields are expected to account for a large percentage of the force. Simulations of the electrostatic force that include a more complex geometry are presently ongoing.

6. CONCLUSIONS

Simple theory of the dual-mass resonator indicated that designs were possible that were insensitive to strain and damping.

Operation of the dual-mass oscillator was demonstrated with a prototype structure. Mechanical amplification was observed at antiresonance. Measurements of the dual-mass oscillator were compared to the design calculations. The antiresonant frequencies were close to calculated values. It was difficult to compare the measured resonant frequencies to the calculated values. Spring softening was time varying using the single-sided drive configuration and the resonant frequencies were sensitive to changes in k_1 , particularly f_{oh} . The measured steady-state absorber mass amplitude was significantly greater than the computer simulated results. The discrepancy was attributed to the electrostatic force expression used in the computer calculations that neglected fringe fields.

The drive mass clamped to the drive electrodes for drive voltages less than 5 Volt due to a design oversight. Spring softening in the drive mass springs was not considered. Future designs will include stiffer drive mass springs. Despite the limited oscillation amplitudes, displacements of greater than 1/3 of the electrode gap were demonstrated with the dual-mass oscillator. Clamping to the substrate was observed when the double-sided drive was used. Protective conductive layers under the drive mass beams implemented in future designs should solve this problem.

ACKNOWLEDGEMENTS

The authors would like to acknowledge the entire staff of the Microelectronics Development Lab at Sandia National Laboratories. None of this work would have been possible without their processing skill and expertise. The authors would also like to acknowledge Dr. Scott Habermehl and Dr. Murat Okandan for sharing their knowledge of the properties of silicon-rich silicon nitride.

This work was supported by the United States Department of Energy under Contract DE-AC04-94AL85000. Sandia is a multiprogram laboratory operated by Sandia Corporation, a Lockheed Martin Company, for the United States Department of Energy.

REFERENCES

1. J. P. Den Hartog, *Mechanical Vibrations*, McGraw Hill, New York, 1956.
2. Tilmans, H. A. C. and Legtenberg, R., "Electrostatically Driven Vacuum-Encapsulated Polysilicon Resonators, Part II. Theory and Performance," *Sensors and Actuators A* 45 (1994) 67-84.
3. Takashi Usuda, "Operational Characteristics of Electrostatically Driven Torsional Resonator With Two Degrees of Freedom," *Sensors and Actuators A* 64 (1998) 255-257.
4. William T. Thompson, *Theory of Vibration with Applications*, 2nd ed., Prentice Hall, New Jersey, 1981.
5. See www.sandia.gov/Micromachine for more information.
6. Kuehnel, Wolfgang, "Modelling of the Mechanical Behaviour of a Differential Capacitor Acceleration Sensor," *Sensors and Actuators A* 48 (1995) 101-108.